An Analytical Solution to the Extended Navier–Stokes Equations Using the Lambert *W* Function*

Aditya Jaishankar and Gareth H. McKinley
Hatsopoulos Microfluids Laboratory, Dept. of Mechanical Engineering, Massachusetts Institute of Technology,
Cambridge, MA 02139

DOI 10.1002/aic.14407

Microchannel gas flows are of importance in a wide range of microelectro mechanical devices. In these flows, the mean free path of the gas can be comparable to the characteristic length of the microchannel, leading to strong diffusion-enhanced transport of momentum. Numerical solutions to the extended Navier–Stokes equations (ENSE) have successfully modeled such microchannel flows. Analytical solutions to the ENSE for the pressure and velocity fields using the Lambert W *function are derived. We find that diffusive contributions to the total transport are only dominant for low average pressures and low pressure drops across the microchannel. For large inlet pressures, we show that the expressions involving the Lambert W function predict steep gradients in the pressure and velocity localized near the channel exit. We extract a characteristic length for this boundary layer. Our analytical results are validated by numerical and experimental results available in the literature.* © 2014 American Institute of Chemical Engineers *AIChE J*, 60: 1413–1423, 2014

Keywords: extended Navier–Stokes equations, Lambert W function, rarefied gas flow, microchannel, microelectro mechanical systems, Knudsen number

Introduction

Microchannel gas flows have elicited much research interest in recent years.[1] Such flows are frequently encountered in microelectro mechanical systems (MEMS) such as in thermal cooling systems for electronic devices,[2] air damping of MEMS resonators,[3,4] gas chromatograph analyzers,[5] and other applications. Theoretical understanding of macroscale fluid flows, where the continuum approximation holds, has existed for many decades and phenomena appearing at these length scales are well understood and described in classic textbooks.[6,7] Microchannel flows, however, exhibit many significant deviations from the predictions of the classical Navier–Stokes equations (CNSE) used to analyze macroscale flows. It has been known from the time of Maxwell[8] that the no-slip boundary condition can be violated in rarefied gas flows. Other deviations from classical macroscale flows include observations of higher mass flow rates through the channel[9] and nonlinear pressure drops along the channel.[10] In a comprehensive overview of the first 50 years of Transport Phenomena,[11] Bird highlights as some of the present day challenges: "(e) What boundary and interfacial conditions in transport phenomena need to be clarified by use of molecular dynamics?" and "(h) What is the correct velocity boundary condition at the tube wall when a homogeneous mixture is flowing through the tube?"

Deviations from the classical results arise from rarefaction of the gas or the shrinking of the characteristic length scales of the flow geometry so that the mean free path λ of the gas becomes comparable to the characteristic length of the flow channel h.[12] Another important source of the deviation of microscale flows from CNSE predictions is the relative importance of wall effects. The shrinking characteristic length scales of the channel lead to increasing surface to volume ratios, and hence, the nature of interaction of the wall with the gas can strongly influence the flow properties. This is essentially a breakdown of the continuum approximation; to be able to neglect microscopic statistical fluctuations, we need a sampling volume with a characteristic length much bigger than the length scale h of the microchannel.

We quantify the deviation from the continuum approximation with the help of the Knudsen number Kn defined as

$$\mathrm{Kn}=\frac{\lambda}{h} \tag{1}$$

where h is the characteristic length of the channel, and λ is the mean free path of the gas defined as[13]

$$\lambda=\frac{\mu}{P}\sqrt{\frac{\pi RT}{2}} \tag{2}$$

Here, μ is the viscosity of the gas, P is the pressure, R is the gas constant, and T is the absolute temperature. In order of increasing Kn, the flow characteristics may be classified as a classical continuum flow, slip flow, transition flow, or a free molecular flow.[12] Some typical values of Kn corresponding to these regimes are shown in Figure 1, which has been adapted from Dongari et al.[14]

Correspondence concerning this article should be addressed to G. H. McKinley at gareth@mit.edu.

*Dedicated to Professor R. B. Bird on the occasion of his 90th birthday.

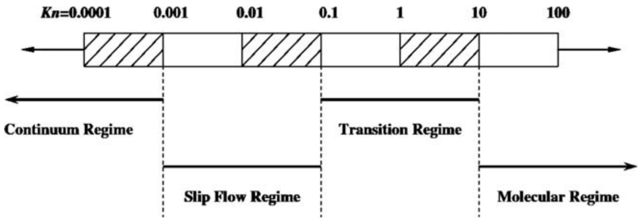

Figure 1. The different regime classifications of microchannel flows based on Knudsen number Kn.

Figure is reproduced from Ref. 14. Permission to reproduce figure granted by Springer.

Some of the earliest attempts to account for wall effects and to model the effects of slip in rarefied gas flows are due to Maxwell,[8] who modeled the wall surfaces as being intermediate between perfectly reflecting and perfectly absorbing. Due to the roughness of the wall, a fraction σ of the gas molecules impacting it are absorbed by the wall, and subsequently re-emitted in a diffuse manner with a velocity distribution corresponding to a quiescent gas at that particular temperature. The remaining fraction $1-\sigma$ is reflected specularly. With this assumption, Maxwell showed that the tangential slip velocity at the wall is given by

$$u_{\mathrm{slip}}=\frac{2-\sigma}{\sigma}\lambda\frac{\partial u}{\partial y} \tag{3}$$

where $\partial u/\partial y$ is the velocity gradient normal to the flow direction. For high Knudsen number flows, deviations from a first-order derivative model are observed, and hence higher order derivatives are frequently used to model slip in microchannel flows.[12,13,15,16] Extensive reviews on the topic of wall slip and rarefied gas flows in microchannels are available.[17]

It has been argued that using the CNSE together with the Maxwell slip velocity formulation is largely an empirical approach to modeling microchannel gas flows.[18] Furthermore, it does not account for local gradients in density which can create local fluxes due to self diffusion.[19,20] A new approach has been proposed in a series of publications by Durst and coworkers (see, e.g., Refs. 14,20–22). The underlying assumption in this theory is that the pressure gradient in the direction of the compressible flow provides an additional diffusive mode of mass transport, which is accounted for analytically by adding an extra term to the CNSE. One, therefore, eliminates the need to include, in an *ad hoc* manner, the Maxwell slip velocity.[14]

A treatment for the self diffusion of gases has been discussed in the landmark transport phenomena text by Hirschfelder et al.[23] They note that in addition to the familiar sources of momentum and mass diffusion that arise from concentration gradients in a multicomponent system, there is another contribution to the diffusive flux that arises from the pressure gradient itself. The coefficients of self diffusion can be experimentally measured using, for example, the diffusion of one isotope of a gas into another, if the molecules are sufficiently heavy (see the discussion by Slattery and Bird[24]). These additional modes of transport are accounted for using a rigorous kinetic theory approach, making the mass flux expression significantly more complicated (see, e.g., p. 516 of Hirschfelder et al.[23]). These additional contributions cannot be neglected when large pressure gradients exist in a rarefied gas flow field. The extended Navier–Stokes equations (ENSE) proposed by Durst et al.[21] account for this mass and momentum transport due to self diffusion by replacing the velocity in the CNSE with a total velocity that is a sum of convective and diffusive velocity terms.

The problem of pressure driven flow of a compressible viscous gas through a tube is posed as a detailed exercise (2B.9) in Bird's second edition of Transport Phenomena.[6] Here, it is suggested that there is an additional contribution to the mass flux along the channel that arises from slip at the wall of the channel. It is suggested (based on empirical evidence) that the slip varies inversely with the pressure in the gas (consistent with Eqs. 2 and 3). The general form of the mass flux variation with pressure is sketched in a figure (Figure 2B.9 of Ref. 6), and the insightful student might ask why the sketch shows not just an augmentation in the total flow rate through the channel but also a nonmonotonic variation. To quantify and understand such observations, it is necessary to have an analytic expression for the mass flux which describes the underlying transport phenomena.

In this article, we provide for the first time analytical results obtained for microchannel gas flows modeled using the ENSE under the assumptions of the lubrication approximation; currently only semi-analytical or numerical solutions are typically reported. Our presentation is intended to be didactic; we first provide a brief overview of the formulation of the model and the relevant equations. We then present the new analytical expression for the relationship between the total mass flux and the applied pressure difference, and discuss the inherent nonmonotonicities and nonlinearities that arise. We also compare the results with experimental data to test their predictive ability. The utility of an analytic description of the flow field is demonstrated using this new formulation to understand the boundary layer structure that can develop near the microchannel exit for sufficiently large inlet pressures. Finally, we use this detailed analytical understanding of this canonical fluid mechanics problem to construct a new flow state map for channel flows of a rarefied gas.

The Extended Navier–Stokes Equations

At steady state and in the absence of any temperature gradients, the system of equations for a single species referred to for compactness as the ENSE are given by[25]

$$\frac{\partial(\rho u_i^{\mathrm{T}})}{\partial x_i}=0 \tag{4}$$

$$\frac{\partial}{\partial x_i}\left(\rho u_i^{\mathrm{T}} u_i^{\mathrm{T}}\right)=-\frac{\partial P}{\partial x_j}-\frac{\partial}{\partial x_i}\left(\tau_{ij}^{C}-\frac{2}{3}\delta_{ij}\dot{m}_k^{\mathrm{D}}u_k^{\mathrm{C}}\right) \tag{5}$$

$$\tau_{ij}^{\mathrm{C}}=-\mu\left(\frac{\partial u_i^{\mathrm{C}}}{\partial x_j}+\frac{\partial u_j^{\mathrm{C}}}{\partial x_i}\right)+\frac{2}{3}\mu\delta_{ij}\frac{\partial u_k^{\mathrm{C}}}{\partial x_k} \tag{6}$$

along with the ideal gas equation of state

$$\rho=\frac{P}{RT} \tag{7}$$

It is assumed that the total mass transport in the extended model consists of a linear sum of convective and diffusive terms. The superscripts C, D, and T in the above equations refer to convective, diffusive, and total quantities, respectively. The total velocity component in the i direction is given by $u_i^{\mathrm{T}}=u_i^{\mathrm{C}}+u_i^{\mathrm{D}}$. The subscripts i, j, k refer to orthogonal coordinate directions and take the values 1, 2, or 3. The other symbols in the above equations are the local density $\rho(\vec{x})$, the local velocity $u(\vec{x})$, the local pressure $P(\vec{x})$, the local dynamic viscosity μ, and the self-diffusive mass flux in the k direction $\dot{m}_i^{\mathrm{D}}=\rho u_i^{\mathrm{D}}$. The Kronecker delta function is denoted by δ_{ij}. The self-diffusive velocity in the i direction is given by the expression

$$u_i^{\mathrm{D}}=-\frac{\mu}{\rho P}\frac{\partial P}{\partial x_i} \tag{8}$$

This diffusive velocity u^{D} is driven by gradients in the pressure and accounts for the Maxwellian slip-like velocity in a natural way, rather than introducing tunable parameters such as the parameter σ in Eq. 3.

In this article, we consider a rectangular microchannel of length L, width w, and height h, with $h \ll w \ll L$. The lubrication approximation holds under these limits[7] and, assuming steady-state flow, the ENSE simplify to[22]

$$\frac{\partial}{\partial x}\left(\rho u^{\mathrm{T}}\right)+\frac{\partial}{\partial y}\left(\rho v^{\mathrm{T}}\right)=0 \tag{9}$$

$$\frac{\partial^2 u^{\mathrm{T}}}{\partial y^2}\approx\frac{1}{\mu}\frac{\partial P}{\partial x} \tag{10}$$

along with the empirical boundary conditions

$$u^{\mathrm{T}}\big|_{y=\pm h}=-\frac{\mu}{\rho P}\frac{\partial P}{\partial x} \tag{11}$$

where the walls of the microchannel are located at $y=\pm h$. These boundary conditions arise from the assumption that the no-slip boundary condition applies to the convective velocity u^{C} at the wall surfaces ($u^{\mathrm{C}}=0$) so that only a diffusive flux is present locally. It is important to note within the lubrication approximation the mass and momentum equations are not satisfied exactly. We ignore terms of order $O(h/L)^2$ and higher. This is a good approximation given the dimensions of the microchannel, and that $h \ll w \ll L$.

Solving Eq. 10 for u^{T} and using the boundary condition (11), Adachi et al.[22] show that

$$\dot{m}^{\mathrm{T}}=\rho u^{\mathrm{T}}=-\frac{\rho}{2\mu}\left(h^2-y^2\right)\frac{dP}{dx}-\frac{\mu}{P}\frac{dP}{dx} \tag{12}$$

where $\dot{m}^{\mathrm{T}}$ is the local mass flux per unit area and the total mass flow rate $\dot{M}^{\mathrm{T}}$ through any cross section of the channel is given by

$$\dot{M}^{\mathrm{T}}=w\int_{-h}^{h}\rho u^{\mathrm{T}}dy \tag{13}$$

$$=-2hw\left(\frac{h^2P}{3\mu RT}+\frac{\mu}{P}\right)\frac{dP}{dx} \tag{14}$$

We now proceed to find analytical expressions for the pressure field and the mass flow rate as well as the velocity field $u(x,y)$ in the channel. To the best of our knowledge, we present the first analytical solutions to the ENSE for flow through a rectangular microchannel. Although an expression for the total mass flux through the channel may be found by solving equation 14 implicitly,[22] previous approaches have solved for the explicit local pressure and velocity fields numerically.

Results and Discussion

Consider the expression for the total mass flow rate $\dot{M}^{\mathrm{T}}$ derived in Eq. 14. Because the mass flow rate remains constant through any arbitrary cross-section of the channel, we have $d\dot{M}^{\mathrm{T}}/dx=0$ and we can write this expression in the form

$$\left(\frac{h^2P}{3\mu RT}+\frac{\mu}{P}\right)\frac{dP}{dx}=-C' \tag{15}$$

where $C'=\dot{M}^{\mathrm{T}}/2hw$ is a constant of integration. This equation can be solved for P implicitly, and we determine C' from the boundary conditions at the inlet and outlet of the channel $P(0)=P_{\mathrm{i}}$ and $P(L)=P_{\mathrm{o}}$ to obtain

$$C'=\frac{1}{6RT}\frac{h^2}{L}\left(P_{\mathrm{i}}^2-P_{\mathrm{o}}^2+\frac{3\mu^2RT}{h^2}\ln\frac{P_{\mathrm{i}}^2}{P_{\mathrm{o}}^2}\right) \tag{16}$$

We now nondimensionalize Eq. 15 using $\bar{x}=x/L$ and $\bar{P}=P/P_{\mathrm{c}}$ where L is the length of the microchannel and P_{c} is a characteristic pressure for an ideal gas given by $P_{\mathrm{c}}=\mu\sqrt{3RT}/h$. As the pressure is increased to P_{c}, the mean free path given by Eq. 2 decreases to give a characteristic mean free path λ_{c} or, equivalently, a characteristic Knudsen number given by $\mathrm{Kn}_{\mathrm{c}}=\lambda_{\mathrm{c}}/h=\sqrt{\pi/6}$ which characterizes the transition region in Figure 1. Substituting these scalings into Eqs. 15 and 16 results in the simpler expression

$$\left(\bar{P}+\frac{1}{\bar{P}}\right)\frac{d\bar{P}}{d\bar{x}}=-\bar{C} \tag{17}$$

where $\bar{C}=(L/\mu)C'$ is dimensionless. Solving this equation for the dimensionless pressure distribution along the channel $\bar{P}(\bar{x})$ with $\bar{P}=P_{\mathrm{i}}/P_{\mathrm{c}}=\bar{P}_{\mathrm{i}}$ at $\bar{x}=0$ and $\bar{P}=P_{\mathrm{o}}/P_{\mathrm{c}}=\bar{P}_{\mathrm{o}}$ at $\bar{x}=1$ we obtain the implicit expression

$$\bar{P}_{\mathrm{i}}^2-\bar{P}^2+\ln\frac{\bar{P}_{\mathrm{i}}^2}{\bar{P}^2}=\left(\bar{P}_{\mathrm{i}}^2-\bar{P}_{\mathrm{o}}^2+\ln\frac{\bar{P}_{\mathrm{i}}^2}{\bar{P}_{\mathrm{o}}^2}\right)\bar{x} \tag{18}$$

At this point, expression (18) can be evaluated using a suitable nonlinear equation solver or root finding algorithm; however, additional insight can be gained by seeking an analytic expression for $\bar{P}(\bar{x})$. This equation admits itself to a closed form analytical solution given by

$$\frac{P(x/L)}{P_{\mathrm{c}}}\equiv\bar{P}(\bar{x})=\sqrt{W\left(\exp\left[-\left(\bar{P}_{\mathrm{i}}^2-\bar{P}_{\mathrm{o}}^2+\ln\frac{\bar{P}_{\mathrm{i}}^2}{\bar{P}_{\mathrm{o}}^2}\right)\bar{x}+\bar{P}_{\mathrm{i}}^2+\ln\bar{P}_{\mathrm{i}}^2\right]\right)} \tag{19}$$

where $W(x)$ is the Lambert W function defined to be the function $W(x)$ that satisfies the equation

$$W(x)\exp\left[W(x)\right]=x \tag{20}$$

Although it may not be widely known, the Lambert W function is ubiquitous in nature and appears in the solution of a number of mathematical as well as physical problems such as electrostatics, population growth, enzyme kinetics, and quantum mechanics. It is similar to the trigonometric functions in the sense that it has no explicit closed form, but a very large number of physical problems are solved with relative ease using it in the solution.[26] Furthermore, almost all popular physical computing packages such as Mathematica, Matlab, and Maple include full support for the Lambert W function, and utilize efficient algorithms to calculate its value at any point in its domain. Corless et al.[27] provide an excellent summary of the history and applications of $W(x)$.

We may now find explicit solutions for the total mass flow rate $\dot{M}^{\mathrm{T}}$ and the velocity profile u^{T} by substituting Eq. 19 into Eqs. 14 and 12, respectively, to obtain

$$\dot{M}^{\mathrm{T}}=\frac{\mu h\omega}{L}\left[\bar{P}_{\mathrm{i}}^{2}-\bar{P}_{\mathrm{o}}^{2}+\ln\left(\frac{\bar{P}_{\mathrm{i}}}{\bar{P}_{\mathrm{o}}}\right)^{2}\right] \tag{21}$$

$$u^{\mathrm{T}}(\bar{x},\bar{y})=\frac{h\sqrt{3RT}}{4L}\frac{\bar{P}(\bar{x})}{[1+\bar{P}^{2}(\bar{x})]}\left(\bar{P}_{\mathrm{i}}^{2}-\bar{P}_{\mathrm{o}}^{2}+\ln\frac{\bar{P}_{\mathrm{i}}^{2}}{\bar{P}_{\mathrm{o}}^{2}}\right)\left(1-\bar{y}^{2}+\frac{2}{3\bar{P}^{2}(\bar{x})}\right) \tag{22}$$

where $\bar{y}=y/h$. To find $u^{\mathrm{T}}(\bar{x})$, we were required to find an analytical expression for the pressure drop $d\bar{P}/d\bar{x}$ (cf. Eq. 12). We give an explicit expression for the pressure drop later; here, we simply note that to find $u^{\mathrm{T}}(\bar{x})$, we have used the fact that the derivative $W'(x)$ of the Lambert function is given by[27]

$$W'(x)=\frac{W(x)}{x(1+W(x))};x\neq 0 \tag{23}$$

We can now also find the individual contributions to the total mass flux that arise from the diffusive velocity field $u^{\mathrm{D}}(\bar{x})$ and the convective velocity field $u^{\mathrm{C}}(\bar{x},\bar{y})$ from Eq. 8

$$u^{\mathrm{D}}(\bar{x})=\bar{P}_{\mathrm{o}}^{2}\frac{h\sqrt{3RT}}{6L}\left(\frac{\mathcal{P}^{2}-1+(1/\bar{P}_{\mathrm{o}}^{2})\ln\mathcal{P}^{2}}{\bar{P}(\bar{x})(1+\bar{P}^{2}(\bar{x}))}\right) \tag{24}$$

$$u^{\mathrm{C}}(\bar{x},\bar{y})=\bar{P}_{\mathrm{o}}^{2}\frac{h\sqrt{3RT}}{4L}\left(\frac{\bar{P}(\bar{x})}{1+\bar{P}^{2}(\bar{x})}\right)\left(\mathcal{P}^{2}-1+(1/\bar{P}_{\mathrm{o}}^{2})\ln\mathcal{P}^{2}\right)\left(1-\bar{y}^{2}-\frac{1}{3\bar{P}^{2}(\bar{x})}\right) \tag{25}$$

in which $\mathcal{P}=\bar{P}_{\mathrm{i}}/\bar{P}_{\mathrm{o}}$.

For a long narrow channel with $h \ll w$, the pressure gradient is unidirectional (along the channel) and the diffusive contribution does not vary across the channel. The total velocity field in the microchannel is given by $u^{\mathrm{T}}(\bar{x},\bar{y})=u^{\mathrm{C}}(\bar{x},\bar{y})+u^{\mathrm{D}}(\bar{x})$.

Having derived the solution for the pressure field $\bar{P}(\bar{x})$ (which in turn determines the density field $\rho(\bar{x})$) we now seek to determine the quality of the lubrication approximation used to derive these solutions. To this end, we substitute the density field $\rho(x)=P(x)/RT$ and the velocity field $u^{T}(x,y)$ using equations (19) and (22) respectively, into the continuity equation (9) to solve for the transverse component of the velocity field $v^{T}(\bar{x},\bar{y})$, and we obtain

$$v^{T}=-\frac{\mu RTh}{P_{c}4L^{2}}A^{2}\frac{\bar{P}(\bar{x})}{[1+\bar{P}^{2}(\bar{x})]^{3}}(\bar{y}^{3}-\bar{y}) \tag{26}$$

where

$$A=\bar{P}_{i}^{2}-\bar{P}_{o}^{2}+\ln\frac{\bar{P}_{i}^{2}}{\bar{P}_{o}^{2}} \tag{27}$$

Equation (10) was obtained from (5) and (6) by neglecting terms of order $(h/L)^2$. We now estimate the magnitude of these neglected terms *a posteriori* by using the obtained solutions for $P(x)$, $u(x,y)$ and $v(x,y)$. We first write out the x component of the momentum equation without neglecting terms of $O((h/L)^2)$:

$$0=-\frac{\partial P}{\partial x}+\frac{\mu}{3}\left(\frac{\partial^{2}u^{T}}{\partial x^{2}}+\frac{\partial^{2}v^{T}}{\partial x\partial y}\right)+\mu\left(\frac{\partial^{2}u^{T}}{\partial x^{2}}+\frac{\partial^{2}u^{T}}{\partial y^{2}}\right) \tag{28}$$

Because $h \ll L, \frac{\partial^2 u^T}{\partial x^2} \ll \frac{\partial^2 u^T}{\partial y^2}$ and hence we can rewrite the above equation as

$$0=-\frac{\partial P}{\partial x}+\frac{\mu}{3}\frac{\partial^{2}v^{T}}{\partial x\partial y}+\mu\frac{\partial^{2}u^{T}}{\partial y^{2}} \tag{29}$$

Because we have analytical solutions for both $u^T(x, y)$ as well as $v^T(x, y)$ we can calculate the terms $\frac{\mu}{3}\frac{\partial^2 v^T}{\partial x\partial y}$ and $\mu\frac{\partial^2 u^T}{\partial y^2}$ as

$$\mu\frac{\partial^{2}u^{T}}{\partial y^{2}}=A\frac{P_{c}}{L}\left(-\frac{\bar{P}(\bar{x})}{2\left(1+\bar{P}^{2}(\bar{x})\right)}\right) \tag{30}$$

and

$$\frac{\mu}{3}\frac{\partial^{2}v^{T}}{\partial x\partial y}=-\frac{\mu^{2}RT}{12L^{3}P_{c}}(3\bar{y}^{2}-1)A^{3}\left(\frac{\left(5\bar{P}^{2}(\bar{x})-1\right)\bar{P}(\bar{x})}{2\left(1+\bar{P}^{2}(\bar{x})\right)^{5}}\right) \tag{31}$$

To find the relative magnitude of the neglected term in the momentum equation, we divide (31) by (30) and obtain

$$\frac{\frac{\mu}{3}\frac{\partial^{2}v^{T}}{\partial x\partial y}}{\mu\frac{\partial^{2}u^{T}}{\partial y^{2}}}=\frac{1}{36}\left(\frac{h}{L}\right)^{2}(3\bar{y}^{2}-1)A^{2}\left(\frac{\left(5\bar{P}^{2}(\bar{x})-1\right)}{\left(1+\bar{P}^{2}(\bar{x})\right)^{4}}\right) \tag{32}$$

In the next section, we compare our analytic expression with experiments by Maurer et al[28]. In these experiments, h = 0.6 μm and L = 10 cm, leading to $(h/L)^2 \sim O(10^{-11})$. Moreover, for all experimentally accessible parameters, the factor

$$A^{2}\left(\frac{5\bar{P}^{2}(\bar{x})-1}{\left(1+\bar{P}^{2}(\bar{x})\right)^{4}}\right)\ll 10^{11} \tag{33}$$

For example, for typical experimental values of $\bar{P}_{\mathrm{i}}/\bar{P}_{\mathrm{o}}=30$ and $\bar{P}_{\mathrm{i}}=10$ used by Maurer et al., the magnitude of this term is about $10^{3} \ll 10^{11}$. Therefore we are justified in employing the lubrication approximation for typical microchannel geometries over a wide range of magnitudes of the dimensionless pressure field. This conclusion is further supported in the next section by comparing the predictions of our results with experimental data.

Comparison with data

Equipped with these analytical solutions for the mass flow rate, the pressure field as well as the local velocity field, we next examine the behavior of these expressions under various conditions of inlet and outlet pressures and also compare the analytic expressions with experimental data. In Figure 2, we show the scaled pressure $\Delta\bar{P}_{\mathrm{s}}=(\bar{P}-\bar{P}_{\mathrm{o}})/(\bar{P}_{\mathrm{i}}-\bar{P}_{\mathrm{o}})$ calculated using Eq. 19 as a function of position along the channel $\bar{x}$. The curves correspond to different values of the inlet pressure $\bar{P}_{\mathrm{i}}$ for a fixed (small) value of the outlet pressure $\bar{P}_{\mathrm{o}}$. It is observed that the nature of the scaled pressure drop $\Delta\bar{P}_{\mathrm{s}}$ strongly depends on the relative values of inlet and outlet pressures. We know that in the classical case the scaled pressure along the channel varies as $\Delta\bar{P}_{\mathrm{s}}=1-\bar{x}$, and this linear result is independent of the inlet and outlet pressures $\bar{P}_{\mathrm{i}}$ and $\bar{P}_{\mathrm{o}}$. Accounting for diffusive terms makes the pressure drop highly nonlinear, and it is now a function of both $\bar{P}_{\mathrm{i}}$ and $\bar{P}_{\mathrm{o}}$. Moreover, for a fixed value of $\bar{x}$, say $\bar{x}=0.5$, can be noted that the value of the scaled pressure varies nonmonotonically at small values of $\bar{P}_{\mathrm{i}}$ and saturates at high values of $\bar{P}_{\mathrm{i}}$.

In this manuscript, although we obtain the pressure profiles presented in figure 2 using a lubrication approximation

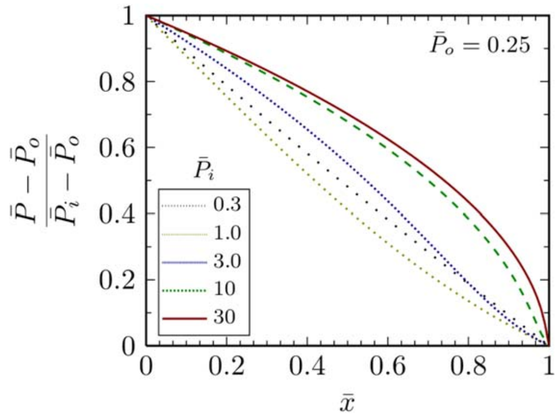

Figure 2. Evolution in the nondimensional pressure $\bar{P}(\bar{x})=P(\bar{x})/P_c$ as a function of nondimensional position $\bar{x}=x/L$ along the microchannel analytically determined from Eq. 19.

We observe that the scaled pressure saturates for high inlet pressures $\bar{P}_\mathrm{i}$. Furthermore, an inflection point is present in the curves, some of which are not readily apparent in the plots above on account of being very close to the exit. [Color figure can be viewed in the online issue, which is available at wileyonlinelibrary.com.]

solution to the simplified ENSE, there are other techniques to arrive at an approximate analytic solution for microchannel gas flows. One widely used approach that has led to much success is to obtain a solution for the full Navier-Stokes equations for a compressible fluid using a regular perturbation method[29]. Notably, Venerus and Bugajsky[30] derive expressions for stream-wise as well as transverse pressure and velocity fields for microchannel flows of compressible fluids, and their analytical results agree well with previously published experimental data. However the authors note explicitly that they assume flow conditions such that Kn $\leq 10^{-3}$ (as opposed to Kn ~ 1 in the present work) and any slip effects are negligible. Qin et al.[31] also present a perturbation solution to the compressible Navier Stokes equations, including the case Kn ~ 1 for both short and long channels. The perturbation solution of Arkilic and Schmidt[32] which applies to long channels ($(h/L)^2 \ll$ Kn) is retrieved by Qin et al. in the appropriate limit. Our analytically derived pressure profiles obtained by utilizing the lubrication approximation (figure 2) also agree with those derived using the perturbation solution in these cited works[31,32] in the correct limit. However, Qin et al. introduce two additional material constants corresponding to slip boundary conditions (slip coefficients), which are obtained from the literature. Moreover, it is apparent from their results that there is an approach to a boundary layer like region near the channel exit. No detailed comments or analysis are presented for this boundary layer structure. We discuss boundary layer like flow in the results section.

The nonlinear evolution of the pressure profile predicted by the ENSE is more readily evident in the pressure gradient profiles. A closer examination of the curves in Figure 2 shows the existence of an inflection point along the profile, that is, although the pressure gradient along the channel is always negative, its magnitude may vary nonmonotonically. We can easily determine the pressure gradient along the channel by differentiating Eq. 19 with respect to $\bar{x}$ to obtain

$$\frac{d\bar{P}(\bar{x})}{d\bar{x}} = -\frac{\bar{P}(\bar{x})}{2(1+\bar{P}^2(\bar{x}))}\left(\bar{P}_\mathrm{i}^2-\bar{P}_\mathrm{o}^2+\ln\frac{\bar{P}_\mathrm{i}^2}{\bar{P}_\mathrm{o}^2}\right) \qquad (34)$$

Plotting Eq. 34 in Figure 3 for different values of the dimensionless inlet pressure $\bar{P}_\mathrm{i}$, the nonmonotonicity in the pressure gradient is readily apparent. In fact, we analytically find the location of this inflection point $\bar{x}^\mathrm{i}$ using Eq. 34 by setting $d^2\bar{P}/d\bar{x}^2=0$ to be

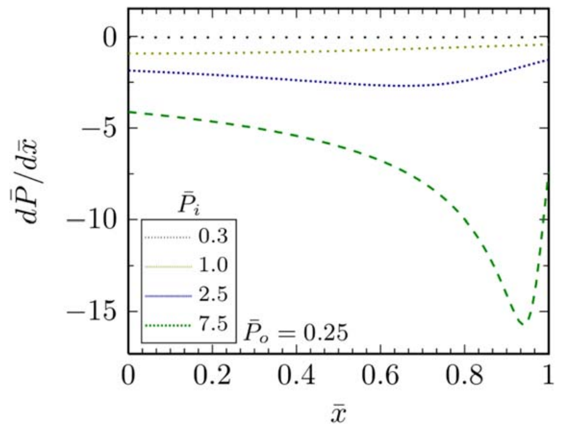

Figure 3. Analytically determined pressure gradient $d\bar{P}/d\bar{x}$ as a function of $\bar{x}$ (Eq. 34) for a fixed value of the outlet pressure.

There exists a point in the channel where the pressure gradient is most favorable (most negative), and the magnitude of the favorable pressure gradient increases with $\bar{P}_\mathrm{i}$. The location $\bar{x}$ at which this occurs is also shifted toward $\bar{x}=1$ as the pressure is increased (cf. Eq. 35). [Color figure can be viewed in the online issue, which is available at wileyonlinelibrary.com.]

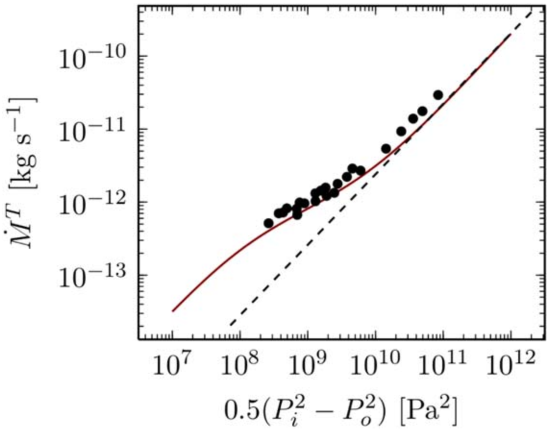

Figure 4. Prediction of the analytically derived solution to the ENSE compared to the experimental measurements taken directly from the values reported by Maurer et al.[28]

The agreement between the prediction and the data is good. The parameters used here are from Maurer et al. $\mu=19.9\times10^{-6}$ Pa s, $h=0.6\mu$m, $w=200\mu$m, $L=10$ cm, $T=293$ K. The outlet pressure was held constant at $P_\mathrm{o}=12$ kPa. The black dashed line shows the CNSE solution for the mass flux. [Color figure can be viewed in the online issue, which is available at wileyonlinelibrary.com.]

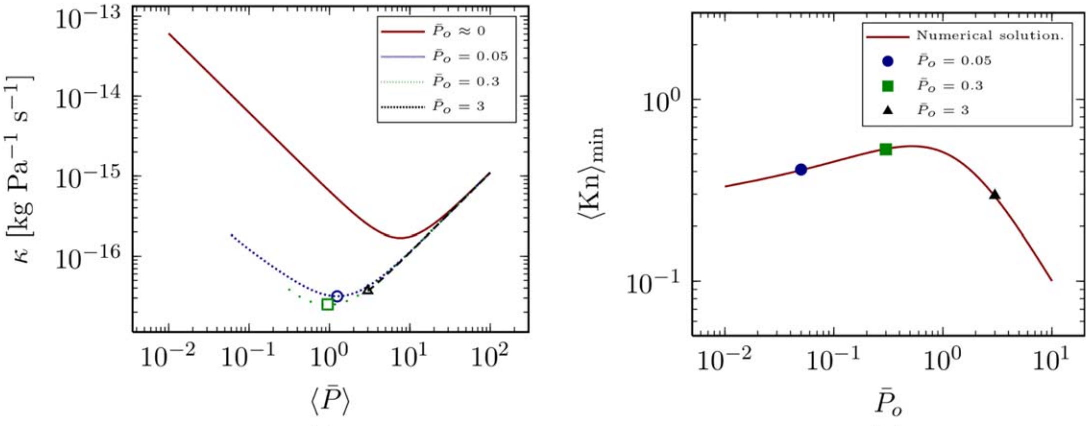

(a) (b)

Figure 5. (a) The conductance κ of the microchannel as a function of the average pressure in the channel.

In contrast to the prediction in the classical case in which the conductance increases linearly with average pressure, the ENSE predicts that the conductance varies nonmonotonically with $\langle \bar{P} \rangle$. (b) The Knudsen number at minimum conductance calculated using the average pressure as a function of outlet pressure. The Knudsen number at minimum conductance varies nonmonotonically with the imposed pressure. [Color figure can be viewed in the online issue, which is available at wileyonlinelibrary.com.]

$$\bar{x}^{\mathrm{i}}=\frac{\bar{P}_{\mathrm{i}}^2+\ln \bar{P}_{\mathrm{i}}^2-1}{\bar{P}_{\mathrm{i}}^2-\bar{P}_{\mathrm{o}}^2+\ln\left(\bar{P}_{\mathrm{i}}^2/\bar{P}_{\mathrm{o}}^2\right)} \tag{35}$$

and the minimum (most negative) pressure gradient in the microchannel $d\bar{P}/d\bar{x}|_{\bar{x}=\bar{x}^{\mathrm{i}}}$, which occurs at the inflection point, is given by

$$\bar{P}'_{\min} \equiv \left.\frac{d\bar{P}}{d\bar{x}}\right|_{\bar{x}=\bar{x}^{\mathrm{i}}} = -\frac{1}{4}\left(\bar{P}_{\mathrm{i}}^2-\bar{P}_{\mathrm{o}}^2+\ln\left(\frac{\bar{P}_{\mathrm{i}}}{\bar{P}_{\mathrm{o}}}\right)^2\right) \tag{36}$$

where the prime denotes differentiation with respect to $\bar{x}$.

Deviations from the classical solution for the mass flow rate of a fluid through a microchannel is a fact that has been experimentally established.[1,10,28,32,33] The mass flow rate is observed to be higher than that predicted by the CNSE with the no-slip boundary condition. This occurs due to the appearance of the additional "slip-like" velocity contribution near the boundaries of the microchannel. This slip-like flow is modeled in the ENSE with the additional diffusive term without the need for introducing any fitting parameters or additional material constants, and hence, this model should be able to predict the higher mass flow rate observed experimentally. Indeed, this is the case; in Figure 4, we compare experimental measurements of the mass flow rate from Maurer et al.[28] with the predictions of the ENSE presented in this article (Eq. 21). The values of channel dimensions and other experimental parameters used in this prediction are the same as those in the work of Maurer et al., and are summarized in the figure caption. We note that the prediction is very good over a wide range of driving pressure differences, and the analytical solutions presented here captures the essential nonlinearities and apparent slip phenomena observed in microchannel flows at moderate Knudsen number.

The conductance

A useful way of representing the overall transport efficiency of the system is in terms of a conductance κ (i.e., the inverse of a flow channel hydrodynamic resistance). For gas flow through a rectangular slit, the ENSE predict that the conductance is given by

$$\kappa \equiv \frac{\dot{M}^{\mathrm{T}}}{\Delta P}=\frac{\mu h w}{L P_{\mathrm{c}}}\frac{1}{\bar{P}_{\mathrm{i}}-\bar{P}_{\mathrm{o}}}\left(\bar{P}_{\mathrm{i}}^2-\bar{P}_{\mathrm{o}}^2+\ln\frac{\bar{P}_{\mathrm{i}}^2}{\bar{P}_{\mathrm{o}}^2}\right) \tag{37}$$

The quantity $\bar{P}_{\mathrm{i}}^2-\bar{P}_{\mathrm{o}}^2$ appears commonly in such problems (e.g., Eq. 37 and the abscissa of Figure 4). Additional insight can be obtained if we rewrite this expression in terms of an average pressure $\langle P\rangle=(P_{\mathrm{i}}+P_{\mathrm{o}})/2$ and a pressure difference $\Delta P=P_{\mathrm{i}}-P_{\mathrm{o}}$ such that $\bar{P}_{\mathrm{i}}^2-\bar{P}_{\mathrm{o}}^2=(\bar{P}_{\mathrm{i}}+\bar{P}_{\mathrm{o}})(\bar{P}_{\mathrm{i}}-\bar{P}_{\mathrm{o}})=2\frac{\langle P\rangle}{P_{\mathrm{c}}}\cdot\frac{\Delta P}{P_{\mathrm{c}}}$. Using these identities, we rewrite the conductance in terms of the average pressure $\langle P\rangle$ of the gas to obtain

$$\kappa=\frac{\mu h w}{L}\left(\frac{2\langle P\rangle}{P_{\mathrm{c}}^2}+\frac{1}{\langle P\rangle-P_{\mathrm{o}}}\ln\left(\frac{2\langle P\rangle-P_{\mathrm{o}}}{P_{\mathrm{o}}}\right)\right) \tag{38}$$

Furthermore, using Eq. 1 and Eq. 2, we can define a Knudsen number $\langle \mathrm{Kn}\rangle$ based on the average inlet pressure as

$$\langle \mathrm{Kn}\rangle=\sqrt{\frac{\pi}{24}\frac{P_{\mathrm{c}}}{\langle P\rangle}} \tag{39}$$

In Figure 5a, we plot the conductance κ as a function of the average dimensionless pressure $\langle \bar{P}\rangle$ in the microchannel. Whereas in the CNSE, the conductance monotonically increases with $\langle \bar{P}\rangle$ (because of the increasing density of the fluid), a distinct nonmonotonicity is apparent in the case of ENSE: the conductance of the channel initially decreases with increasing average pressure and then increases to become indistinguishable from the classical limit. This nonmonotonicity occurs due to the added diffusion transport mechanism. At low pressure differences, diffusive contributions of the flow resulting from the density gradient along the channel are vastly more efficient at transporting mass and momentum through the microchannel compared to classical convective terms. It can be seen from Figure 5a that the location of the minimum conductance (indicated by the symbols) is a function of the outlet pressure $\bar{P}_{\mathrm{o}}$.

In Figure 5b, we plot the value of $\langle \mathrm{Kn}\rangle$ at that value of the outlet pressure for which the conductance is a minimum. Note that we are not able to find a simple analytical solution for the value of $\langle P\rangle$ at minimum conductance due to the nonlinearity in Eq. 38. We, therefore, determine $\langle \mathrm{Kn}\rangle$ as a

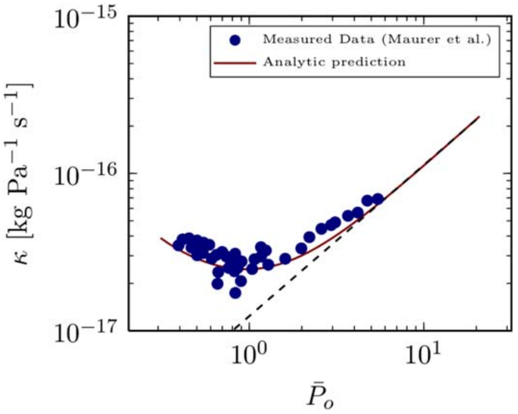

Figure 6. Comparison of the prediction of the analytical expression obtained in the present work for the conductance of a microchannel (Eq. 38) against experimental data obtained by Maurer et al.[28]

The outlet pressure as well as fluid properties and microchannel geometry is the same as that in Ref. 28 The prediction is very good and closely agrees with the experimental data. The black dashed line shows the CNSE solution. [Color figure can be viewed in the online issue, which is available at wileyonlinelibrary.com.]

function of the dimensionless outlet pressure $\bar{P}_\text{o}$ numerically. Here, we notice another nonmonotonicity, and the Knudsen number $\langle \text{Kn} \rangle_\text{min}$ defined using the average pressure at which minimum conductance is obtained first increases with increasing outlet pressure and subsequently decreases as $\langle \text{Kn} \rangle_\text{min} \sim \bar{P}_\text{o}^{-1}$. For larger values of $\bar{P}_\text{o}$ (and hence larger $\langle \bar{P} \rangle$), the variation of conductance κ approaches the classical Navier–Stokes case, and κ increases monotonically with increasing $\langle \bar{P} \rangle$. In this limit, the average pressure at minimum conductance equals $\langle \bar{P} \rangle \approx \bar{P}_\text{i} \approx \bar{P}_\text{o}$.

We can also compare the conductance defined by Eq. 37 with experimental measurements of the mass flux through a microchannel as a function of $P_\text{i}^2 - P_\text{o}^2$. In Figure 6, we plot the experimental measurements of Maurer et al. with the analytic expression in Eq. 37. There are no adjustable parameters in this expression if the inlet and outlet pressures are specified in addition to the channel geometry. It is clear that the ENSE provide an excellent description of the conductance of a rarefied gas through a microchannel, including the appearance of a minimum in the conductance at a specified value of the average pressure $\langle P \rangle = (1/2)(P_\text{i} + P_\text{o})$ and the pressure driving force $\Delta P = P_\text{i} - P_\text{o}$. Also shown on this plot is the CNSE solution (black dashed line), in which κ increases linearly with $\bar{P}_\text{o}$.

Velocity field in the channel

We now turn to the velocity field $u^\text{T}(x,y)$ given by Eq. 22. In Figure 7, we show the nondimensional total velocity $\bar{u}^\text{T}(\bar{x},\bar{y}) = \frac{u^\text{T}}{\mu\sqrt{3RT}/4L}$ at different values of $\bar{x}$, for two different conditions: (a) $\bar{P}_\text{i}=1$ and (b) $\bar{P}_\text{i}=10$, keeping the outlet pressure fixed at $\bar{P}_\text{o}=0.25$. We observe in Figure 7a that the velocity is nonzero at the channel walls, and this slip-like velocity arises from accounting for self diffusion due to local gradients in pressure. In fact, for these values of $\bar{P}_\text{i}$ and $\bar{P}_\text{o}$, the diffusive velocity contribution (given by Eq. 24) is a significant proportion of the total velocity.

This picture changes when the pressure ratio, which we define as $\mathcal{P} = \bar{P}_\text{i}/\bar{P}_\text{o}$, is increased. In Figure 7b, we show the same quantity $\bar{u}^\text{T}(\bar{x},\bar{y})$ with $\bar{P}_\text{i}=10$ and $\bar{P}_\text{o}=0.25$, corresponding to $\mathcal{P}=40$. It is immediately observed that in this case, the convective terms in the velocity largely outweigh the diffusive terms. In this regime, the slip-like velocity is relatively unimportant; this fact has been noted by other researchers, for example, Adachi et al.[22] The diffusive contribution to the mass flow rate is only important if it is of the same order of magnitude as the convective contribution. For this, we require both of the (independently variable) dimensionless pressures $\bar{P}_\text{i}$ and $\bar{P}_\text{o}$ to be small. With increasing $\bar{P}_\text{i}$, the wall boundary condition begins to approach that of no-slip and the velocity profile becomes parabolic. This is reassuring because in the limit of high pressure, the Knudsen number is small (Kn $\ll 1$; cf. Eq. 2), and microscale corrections should become relatively unimportant. However, we also note that because of the compressibility of the gas, there is still a steady increase in the local velocity down the channel in this case as shown in Figure 7b. Moreover, the pressure profile along the microchannel is still highly nonlinear and differs considerably from the CNSE solution, as can be

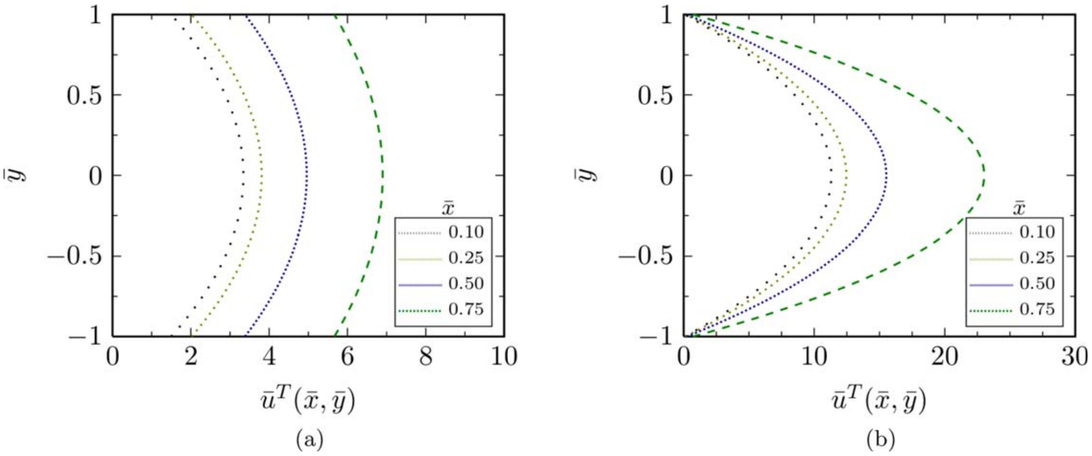

Figure 7. Velocity profiles in the microchannel at different locations $\bar{x}$.

(a) $\bar{P}_\text{i}=1$ and $\bar{P}_\text{o}=0.25(\mathcal{P}=4)$. The contribution of the diffusive velocity terms is a significant proportion of the total velocity and increases along the channel. (b) $\bar{P}_\text{i}=10$ and $\bar{P}_\text{o}=0.25(\mathcal{P}=40)$. In this case, there is still slip at the walls, but its contribution to the total mass flux is negligibly small. [Color figure can be viewed in the online issue, which is available at wileyonlinelibrary.com.]

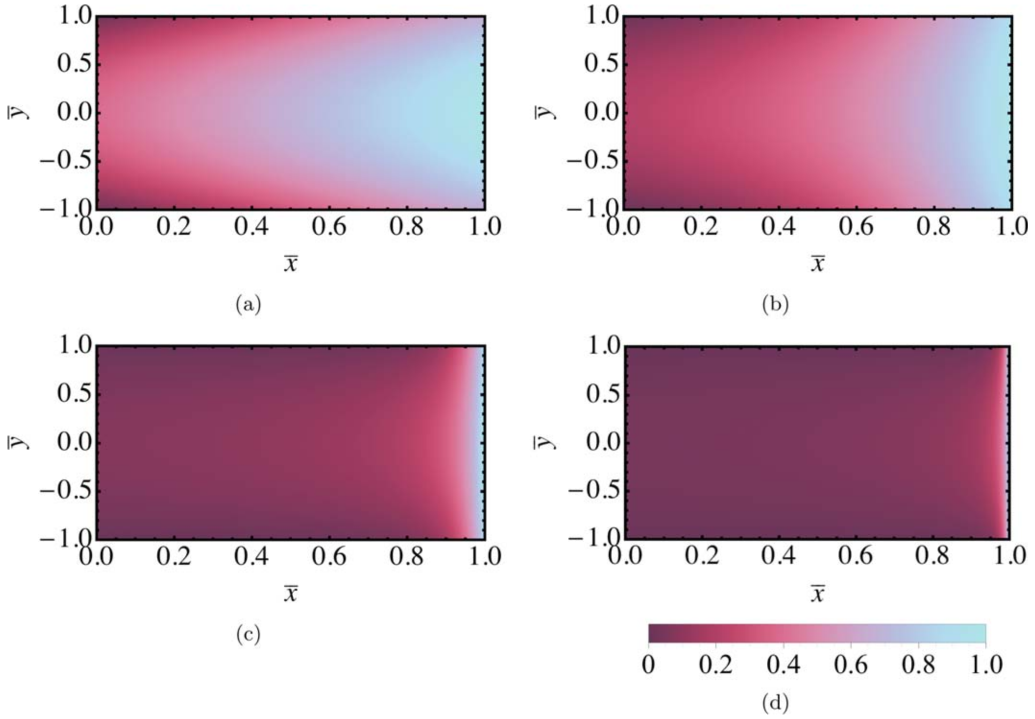

Figure 8. Magnitude of the scaled velocity $\mathcal{U}$ in the microchannel as a function of spatial position for different values of inlet pressure.

(a) $\bar{P}_i=0.3$, (b) $\bar{P}_i=1.0$, (c) $\bar{P}_i=5.0$, and (d) $\bar{P}_i=10$ at fixed outlet pressure $\bar{P}_o=0.25$. For larger values of $\bar{P}_i$, the fluid undergoes a sudden increase in velocity in the vicinity of $\bar{x}=1$. Color scale bar shows values of $\mathcal{U}$ ranging from 0 to 1. [Color figure can be viewed in the online issue, which is available at wileyonlinelibrary.com.]

seen from Figure 2. As we show later, to approach the classical result $\Delta\bar{P}=1-\bar{x}$, we require both $\mathcal{P}\to 1$ and $P_i \gg P_c$.

To better visualize the evolution in the velocity field along the channel, we consider the quantity $\mathcal{U}(\bar{x},\bar{y})$, which we call the scaled velocity, defined as

$$\mathcal{U}(\bar{x},\bar{y})=\frac{u^{T}(\bar{x},\bar{y})-u^{T}_{\min}}{u^{T}_{\max}-u^{T}_{\min}} \tag{40}$$

where $u^{T}_{\min}$ and $u^{T}_{\max}$ are the minimum and maximum velocities in the microchannel. It is clear from Figures 7a, b that the minimum and maximum velocities lie somewhere along the $\bar{y}=\pm1$ and $\bar{y}=0$ lines, respectively. This is also readily seen from Eq. 22; if we isolate the terms in Eq. 22 that depend on $\bar{x}$ and rewrite it as

$$u^{T}=\xi_1\frac{\bar{P}(\bar{x})}{1+\bar{P}^2(\bar{x})}\left(\xi_2+\frac{2}{3\bar{P}^2(\bar{x})}\right) \tag{41}$$

where $\xi_1>0$ and $\xi_2\geq 0$ are coefficients independent of $\bar{x}$, and $\bar{P}(\bar{x})$ is given in terms of the Lambert W function. We can show that u^{T} is a strictly increasing function of $\bar{x}$ (because the pressure $\bar{P}(\bar{x})$ is a strictly decreasing function of $\bar{x}$.). Therefore, the minimum velocity in the channel is at $(\bar{x}=0,\bar{y}=\pm1)$, whereas the maximum in the velocity occurs at $(\bar{x}=1,\bar{y}=0)$, which can now easily be found for any choice of $\bar{P}_i$ and $\bar{P}_o$.

Figures 8a–d show shaded plots of the scaled velocity $\mathcal{U}(\bar{x},\bar{y})$ as a function of the dimensionless channel coordinates. Each panel corresponds to a different value of $\bar{P}_i$ and the value of the outlet pressure was held to be constant at $\bar{P}_o=0.25$. We observe that as the driving pressure difference is increased, the scaled velocity increases much more steeply in the vicinity of $\bar{x}\approx 1$.

This behavior can be rationalized from the pressure gradient profiles presented in Figure 3; as $\bar{P}_i$ is increased, the magnitude of the pressure gradient along the channel increases rapidly. In addition, Eq. 35 shows that in the limit of large pressure ratios $\mathcal{P}=\bar{P}_i/\bar{P}_o$, the location of the maximum favorable pressure gradient tends toward $\bar{x}^{i}\to 1$. This leads to the rapid increase of the gas velocity in the vicinity of $\bar{x}=1$ for large $\mathcal{P}$. To better visualize this sudden change in the velocity near the outlet, in Figure 9, we present line

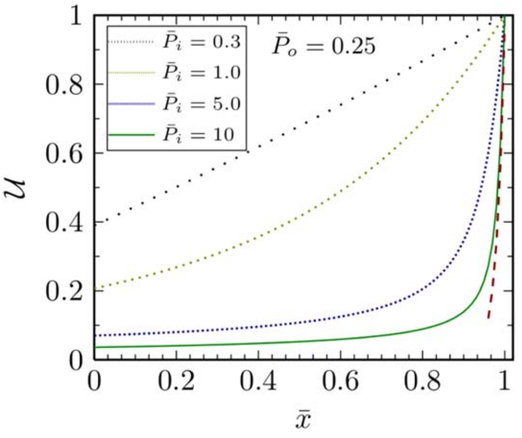

Figure 9. Scaled profiles of the centerline velocity along the microchannel for different values of $\bar{P}_i$.

Increasing $\bar{P}_i$ leads to a steep increase in the scaled velocity close to $\bar{x}=1$. The red dashed line shows the boundary layer approximation given in Table 1 for $\bar{P}_i=10\gg 1$, $\bar{P}_o=0.25\ll 1$. [Color figure can be viewed in the online issue, which is available at wileyonlinelibrary.com.]

scans of the scaled centerline velocity $\mathcal{U}$ at different values of $\bar{P}_{\mathrm{i}}$. The steep increase in the scaled velocity is clearly visible. This behavior stands in stark contrast to the classical incompressible solution, where the pressure gradient and the corresponding centerline velocity are constant throughout the channel.

Boundary layer analysis

The rapid variation in the velocity field close to $\bar{x} \approx 1$ suggests a boundary layer analysis is appropriate when $\mathcal{P} \gg 1$. Through such an analysis, we can extract a characteristic length scale for this boundary layer as well as the asymptotic behavior of pressure and velocity for different limits of $\bar{P}_{\mathrm{i}}$ and $\bar{P}_{\mathrm{o}}$.

We begin by a consideration of Eq. 18 which we reproduce here for clarity, with the pressure ratio $\mathcal{P}$ explicitly indicated

$$\bar{P}_{\mathrm{i}}^2-\bar{P}(\bar{x})^2+\ln\frac{\bar{P}_{\mathrm{i}}^2}{\bar{P}^2(\bar{x})}=\bar{P}_{\mathrm{o}}^2\left(\mathcal{P}^2-1+(1/\bar{P}_{\mathrm{o}}^2)\ln\mathcal{P}^2\right)\bar{x} \qquad (42)$$

Differentiating this equation with respect to $\bar{x}$ we obtain

$$\left(\bar{P}(\bar{x})+\frac{1}{\bar{P}(\bar{x})}\right)\frac{d\bar{P}(\bar{x})}{d\bar{x}}=-\frac{\bar{P}_{\mathrm{o}}^2}{2}\left(\mathcal{P}^2-1+(1/\bar{P}_{\mathrm{o}}^2)\ln\mathcal{P}^2\right) \qquad (43)$$

We now perform the variable transformation $\xi=1-\bar{x}$ and let $\bar{P}(\bar{x})=\bar{P}(1-\xi)=\bar{\psi}(\xi)$. Therefore, Eq. 43 now becomes

$$\left(\bar{\psi}+\frac{1}{\bar{\psi}}\right)\frac{d\bar{\psi}}{d\xi}=\frac{\bar{P}_{\mathrm{o}}^2}{2}\left(\mathcal{P}^2-1+(1/\bar{P}_{\mathrm{o}}^2)\ln\mathcal{P}^2\right) \qquad (44)$$

Note that at $\bar{x}=0$ we have $\xi=1$ and $\bar{\psi}(1)=\bar{P}_{\mathrm{i}}$. Similarly, $\bar{\psi}(0)=\bar{P}_{\mathrm{o}}$. If desired a full matched asymptotic analysis of this equation can be carried out. Here, we are primarily interested in the behavior of the pressure field in the vicinity of the exit of the channel ($\xi \ll 1$), that is, the inner expansion where $\psi(\xi) \approx \bar{P}_{\mathrm{o}}$. We can consider two limits of this nonlinear equation: $\bar{P}_{\mathrm{o}} \ll 1$ and $\bar{P}_{\mathrm{o}} \gg 1$ depending on how large the outlet pressure at the end of microchannel is compared to the characteristic pressure scale $P_{\mathrm{c}}=\mu\sqrt{3RT}/h$. In the former case, Eq. 44 simplifies to

$$\frac{1}{\bar{\psi}}\frac{d\bar{\psi}}{d\xi}\approx\frac{\bar{P}_{\mathrm{o}}^2}{2}\left(\mathcal{P}^2-1+(1/\bar{P}_{\mathrm{o}}^2)\ln\mathcal{P}^2\right) \qquad (53)$$

while for $\bar{P}_{\mathrm{o}} \gg 1$ we obtain

$$\bar{\psi}\frac{d\bar{\psi}}{d\xi}\approx\frac{\bar{P}_{\mathrm{o}}^2}{2}\left(\mathcal{P}^2-1+(1/\bar{P}_{\mathrm{o}}^2)\ln\mathcal{P}^2\right) \qquad (54)$$

These differential equations can be easily solved to find the limiting behavior of the pressure field close to $\bar{x}=1$. These results are presented in Tables 1 and 2.

We can apply a similar approximation of the governing differential equation in the vicinity of the channel exit for the velocity field u^{T}. First, we rewrite Eq. 12 in nondimensional form and apply the same variable transformations described above to obtain

$$u^{\mathrm{T}}=\frac{h\sqrt{3RT}}{2L}\left[1+\frac{2}{3}\frac{1}{\bar{\psi}^2}\right]\frac{d\bar{\psi}}{d\xi} \qquad (55)$$

which in the limits $\bar{P}_{\mathrm{o}} \ll 1$ and $\bar{P}_{\mathrm{o}} \gg 1$ simplify, respectively, to

$$u^{\mathrm{T}}\approx\frac{h\sqrt{3RT}}{3L}\frac{1}{\bar{\psi}^2}\frac{d\bar{\psi}}{d\xi} \qquad (56)$$

and

$$u^{\mathrm{T}}\approx\frac{h\sqrt{3RT}}{2L}\frac{d\bar{\psi}}{d\xi} \qquad (57)$$

We may now substitute into these equations the asymptotic form of the pressure from Tables 1 and 2, according to the relevant magnitude of $\bar{P}_{\mathrm{o}}$, to find the limiting expressions

Table 1. Limiting Expressions for Pressure $\bar{P}(\bar{x})$ and Velocity $u^{\mathrm{T}}(\bar{x})$ for the Case $\bar{P}_{\mathrm{o}} \ll 1$

	$\bar{P}_{\mathrm{o}} \ll 1, \mathcal{P} \sim 1$	$\bar{P}_{\mathrm{o}} \ll 1, \mathcal{P} \gg 1$
$\bar{P}(\bar{x})$	$\bar{P}_{\mathrm{o}}\exp\left[(1/2)(\mathcal{P}^2-1)(1-\bar{x})\right]$ (45)	$\bar{P}_{\mathrm{o}}\exp\left[(1/2)(\bar{P}_0^2(\mathcal{P}^2-1)+\ln\mathcal{P}^2)(1-\bar{x})\right]$ (46)
$u^{\mathrm{T}}(\bar{x})$	$\frac{h\sqrt{3RT}}{6L}\frac{\mathcal{P}^2-1}{\bar{P}_{\mathrm{o}}}\exp\left[-\frac{1}{2}(\mathcal{P}^2-1)(1-\bar{x})\right]$ (47)	$\frac{h\sqrt{3RT}}{6L}\frac{\bar{P}_{\mathrm{o}}^2(\mathcal{P}^2-1)+\ln\mathcal{P}^2}{\bar{P}_{\mathrm{o}}}\exp\left[-\frac{1}{2}(\bar{P}_0^2(\mathcal{P}^2-1)+\ln\mathcal{P}^2)(1-\bar{x})\right]$ (48)

The expressions in the second column, in which $\mathcal{P} \rightarrow 1$, is obtained by expanding the logarithm for $\mathcal{P} \approx 1$. Equation numbers are given within parentheses.

Table 2. Limiting Expressions for Pressure $\bar{P}(\bar{x})$ and Velocity $u^{\mathrm{T}}(\bar{x})$ for the Case $\bar{P}_{\mathrm{o}} \gg 1$

	$\bar{P}_{\mathrm{o}} \gg 1, \mathcal{P} \sim 1$	$\bar{P}_{\mathrm{o}} \gg 1, \mathcal{P} \gg 1$
$\bar{P}(\bar{x})$	$\bar{P}_{\mathrm{o}}\sqrt{(\mathcal{P}^2-1)(1-\bar{x})+1}$ (49)	$\bar{P}_{\mathrm{o}}\sqrt{\left(\mathcal{P}^2-1+\frac{1}{\bar{P}_{\mathrm{o}}^2}\ln\mathcal{P}^2\right)(1-\bar{x})+1}$ (50)
$u^{\mathrm{T}}(\bar{x})$	$\frac{h\sqrt{3RT}}{4L}\frac{\mathcal{P}^2-1}{\bar{P}_{\mathrm{o}}\sqrt{(\mathcal{P}^2-1)(1-\bar{x})+1}}$ (51)	$\frac{h\sqrt{3RT}}{4L}\frac{\bar{P}_{\mathrm{o}}\left(\mathcal{P}^2-1+\frac{1}{\bar{P}_{\mathrm{o}}^2}\ln\mathcal{P}^2\right)}{\sqrt{\left(\mathcal{P}^2-1+\frac{1}{\bar{P}_{\mathrm{o}}^2}\ln\mathcal{P}^2\right)(1-\bar{x})+1}}$ (52)

Although there is no exponential behavior in this case, when $\mathcal{P} \gg 1$, the functional dependence of the expressions for pressure and velocity are such that steep gradients occur near the channel exit. As before, the expressions in the second column, in which $\mathcal{P} \rightarrow 1$, is obtained by expanding the logarithm for $\mathcal{P} \approx 1$. Equation numbers are given within parentheses.

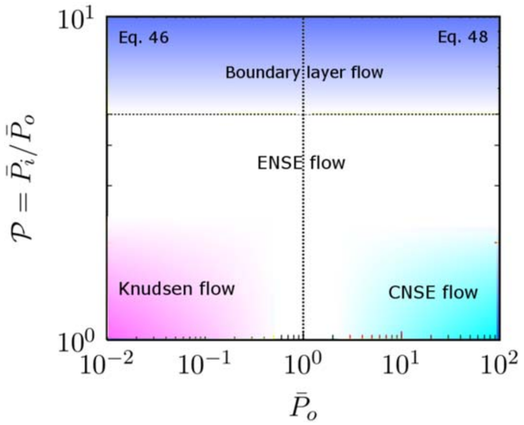

Figure 10. The different flow regimes for microchannel gas flows.

Of note is the boundary layer flow regime, in which steep gradients in the pressure field as well as velocity field are localized in the vicinity of the channel exit. [Color figure can be viewed in the online issue, which is available at wileyonlinelibrary.com.]

for the velocity field in the boundary layer near the exit. These results are also summarized in Tables 1 and 2.

The exponential dependence of both the pressure field as well as the total velocity field on $\bar{x}$ for low outlet pressures $\bar{P}_o \ll 1$ immediately suggests a characteristic length scale δ for the boundary layer region given by

$$\frac{\delta}{L} \sim \frac{1}{\bar{P}_o^2 \mathcal{P}^2 + \ln \mathcal{P}^2} = \frac{3\mu^2 RT}{h^2 P_i^2 + 3\mu^2 RT \ln \left(P_i^2/P_o^2\right)} \tag{58}$$

For a fixed value of the outlet pressure $\bar{P}_o$, the boundary layer thickness decreases with increasing values of the inlet pressure $\bar{P}_i$ and this explains the form of the velocity profiles seen in Figure 9. Equivalently, decreasing $\bar{P}_o$ also decreases the boundary layer thickness, although more slowly than increasing $\bar{P}_i$.

A different structure for the boundary layer at the exit is observed when the outlet pressure is high ($\bar{P}_o \gg 1$). The compressibility of the gas can still be important and there can still be a rapid decrease in the pressure near the exit. In this case, the pressure and velocity profiles have a square root and an inverse square root dependence on the distance from the exit, respectively. However, the length scale of the boundary layer remains the same as that of Eq. 58. The detailed expressions for this case are given in Table 2.

Conclusions

In this article, we present, for the first time, analytical solutions to the ENSE and obtain expressions for the pressure field, mass flow rate, and velocity field for flow through a rectangular microchannel. The ENSE approach models the apparent slip-like flow of rarefied gases in microchannel geometries by accounting for additional diffusive mass transport due to local pressure gradients. Using the analytical expressions derived here using the Lambert W function, the nonlinear behavior of the pressure field and the resulting velocity field was examined in detail. The analytical expressions derived here are able to successfully capture the anomalous mass flow rate increases observed experimentally.

The ability to obtain an analytic expression for the pressure profile $\bar{P}(\bar{x})$ along the channel (19) in terms of the Lambert W function also helps us construct a more detailed version of the regime map that was shown schematically in Figure 1. This new two-dimensional (2-D) map is best represented in terms of the pressure ratio $\mathcal{P}=P_i/P_o=\bar{P}_i/\bar{P}_o$ that is driving the flow and either the average pressure $\langle P \rangle=(1/2)(P_i+P_o)$ in the channel or the scaled outlet pressure $\bar{P}_o=P_o/P_c$, each of which characterizes the thermodynamic state of the gas and the Knudsen number in the channel. We use the latter representation to construct Figure 10. The 2-D velocity profile and the pressure profile along the channel are described by Eqs. 19 and 22 for this entire space. For large outlet pressures ($P_o \gg P_c$) and small pressure drops ($\mathcal{P} \approx 1$), the ENSE for compressible viscous flow at moderate Knudsen numbers collapse to the CNSE. For low average pressures (corresponding to high Knudsen number) and small pressure differences, the flow approaches the Knudsen regime in which ballistic transport dominates. To describe, this regime requires the solution of the Boltzmann equation using appropriate numerical techniques which depend on the Knudsen number range of interest.[13]

As the pressure drop along the channel increases ($\mathcal{P} \gg 1$), the flow develops a boundary layer structure in which the largest velocity changes occur in a thin region of length δ near the channel exit. The specific form of the pressure profile or centerline velocity profile in this boundary layer regime depends on the magnitude of the outlet pressure P_o (compared to the characteristic value P_c). The results for both $P_o \gg P_c$ and $P_o \ll P_c$ are given in Tables 1 and 2, respectively. For extremely high-pressure ratios, additional effects such as inertial acceleration and viscous heating may further modify the velocity field near the exit. The framework and methodology for dealing with such transport effects have been outlined by Bird and coworkers in numerous publications (see, e.g., Refs. 6,11,23) but are beyond the scope of this work.

Acknowledgments

AJ and GHM would like to thank Professor S. K. Das for valuable initial discussions on the Extended Navier-Stokes Equations during his visit to the Department of Mechanical Engineering at MIT as a Peabody Visiting Professor.

Literature Cited

1. Ho CM, Tai YC. Micro-electro-mechanical-systems (MEMS) and fluid flows. *Annu Rev Fluid Mech*. 1998;30(1):579–612.
2. Joo Y, Dieu K, Kim CJ. Fabrication of monolithic microchannels for IC chip cooling. *Proc IEEE*. 1995;6:362–367.
3. Newell WE. Miniaturization of tuning forks. *Science*. 1968;161:1320–1326.
4. Nguyen CTC. Micromechanical resonators for oscillators and filters. *Proceedings of the 1995 IEEE International Ultrasonics Symposium*. Seattle, WA: IEEE, 1995;1:489–499.
5. Terry SC, Jerman JH, Angell JB. A gas chromatographic air analyzer fabricated on a silicon wafer. *IEEE Trans Electron Devices*. 1979;26:1880–1886.
6. Bird RB, Stewart WE, Lightfoot EN. *Transport Phenomena*. New York: Wiley, 1960.
7. Batchelor GK. *An Introduction to Fluid Dynamics*. New York: Cambridge University Press, 1967.
8. Maxwell JC. On stresses in rarified gases arising from inequalities of temperature. *Philos Trans R Soc*. 1879;170:231–256.
9. Harley JC, Huang Y, Bau HH, Zemel JN. Gas flow in micro-channels. *J Fluid Mech*. 2006;284:257–274.
10. Liu J, Tai YC, Ho CM. MEMS for pressure distribution studies of gaseous flows in microchannels. *IEEE International Conference on Micro Electro Mechanical Systems*. Amsterdam, Netherlands: IEEE, 1995:209–215.
11. Bird RB. Five decades of transport phenomena. *AIChE J*. 2004;50(2):273–287.

12. Kandlikar SG, Garimella S, Li D, Colin S, King MR. *Heat Transfer and Fluid Flow in Minichannels and Microchannels*. Oxford: Elsevier, 2006.
13. Hadjiconstantinou NG. The limits of Navier-Stokes theory and kinetic extensions for describing small-scale gaseous hydrodynamics. *Phys Fluids*. 2006;18:111301.
14. Dongari N, Sharma A, Durst F. Pressure-driven diffusive gas flows in micro-channels: from the Knudsen to the continuum regimes. *Microfluid Nanofluid*. 2009;6:679–692.
15. Hadjiconstantinou NG. Comment on Cercignani's second-order slip coefficient. *Phys Fluids*. 2003;15(8):2352.
16. Prabha SK, Sathian SP. Calculation of thermo-physical properties of Poiseuille flow in a nano-channel. *Int J Heat Mass Transfer*. 2013; 58(1–2):217–223.
17. Zhang WM, Meng G, Wei X. A review on slip models for gas microflows. *Microfluid Nanofluid*. 2012;13(6):845–882.
18. Sambasivam R. Extended navier-stokes equations: derivations and applications to fluid flow problems. PhD Thesis, Universitat Erlangen-Nurnberg, Erlangen, 2013.
19. Brenner H. Navier-Stokes revisited. *Phys A: Stat Mech Appl*. 2005; 349(1–2):60–132.
20. Chakraborty S, Durst F. Derivations of extended Navier-Stokes equations from upscaled molecular transport considerations for compressible ideal gas flows: towards extended constitutive forms. *Phys Fluids*. 2007;19(8):088104.
21. Durst F, Gomes J, Sambasivam R. Thermofluiddynamics: do we solve the right kind of equations. *Proceeding of the International Symposium on Turbulence, Heat and Mass Transfer*. Dubrovnik: ICHMT, 2006:25–29.
22. Adachi T, Sambasivam R, Durst F, Filimonov D. Analytical treatments of micro-channel and micro-capillary flows. *3rd Micro and Nano Flows Conference*. Thessaloniki, Greece: Brunel University, 2011:1–10.
23. Hirschfelder JO, Curtiss CF, Bird RB. *Molecular Theory of Gases and Liquids*. New York: Wiley, 1954.
24. Slattery JC, Bird RB. Calculation of the diffusion coefficient of dilute gases and of the self-diffusion coefficient of dense gases. *AIChE J*. 1958;4(2):137–142.
25. Sambasivam R, Chakraborty S, Durst F. Numerical predictions of backward-facing step flows in microchannels using extended Navier-Stokes equations. *Microfluid Nanofluid*. 2013;1–16.
26. Valluri SR, Jeffrey DJ, Corless RM. Some applications of the Lambert W function to physics. *Can J Phys*. 2000;78(9):823–831.
27. Corless RM, Gonnet GH, Hare DEG, Jeffrey DJ, Knuth DE. On the Lambert W function. *Adv Comput Math*. 1996;5:329–359.
28. Maurer J, Tabeling P, Joseph P, Willaime H. Second-order slip laws in microchannels for helium and nitrogen. *Phys Fluids*. 2003;15(9): 2613.
29. Taliadorou EG, Neophytou M, Georgiou GC. Perturbation solutions of Poiseuille flows of weakly compressible Newtonian liquids. *J Non-Newtonian Fluid Mech*. 2009;163:25–34.
30. Venerus DC, Bugajsky DJ. Compressible laminar flow in a channel. *Phys Fluids*. 2010;22:046101.
31. Qin FH, Sun DJ, Yin XY. Perturbation analysis on gas flow in a straight microchannel. *Phys Fluids*. 2007;19:027103.
32. Arkilic E, Schmidt M, Breuer K. Gaseous slip flow in long microchannels. *J Microelectromech Syst*. 1997;6(2):167–178.
33. Pfahler J, Harley J, Bau H, Zemel JN. Gas and liquid flow in small channels. *ASME Dynamic Systems and Controls Conference*, Vol. 32. Atlanta: ASME, 1991;32:49–60.

Manuscript received Oct. 9, 2013, and revision received Jan. 15, 2014.